Assessment of FY-3E GNOS-II GNSS-R Global Wind Product

Feixiong Huang ⓘ, *Member, IEEE*, Junming Xia ⓘ, Cong Yin ⓘ, Xiaochun Zhai ⓘ, Na Xu ⓘ, Guanglin Yang,
Weihua Bai, Yueqiang Sun, Qifei Du, Mi Liao, Xiuqing Hu ⓘ, Peng Zhang ⓘ, Lichang Duan, and Yan Liu

Abstract—**Two different Global Navigation Satellite System (GNSS) Reflectometry wind products are to be developed for the Global Navigation Satellite System Occultation Sounder II (GNOS-II) payload on the FengYun-3E (FY-3E) satellite: A global wind product optimized for global low-to-medium wind speeds and a cyclone wind product optimized for high wind speeds in the tropical and extratropical cyclones. This article presents a comprehensive assessment of the GNOS-II global wind product for both global positioning system (GPS) and Beidou (BDS) product at wind speeds below 25 m/s using its data of first six months. Three datasets, including the European Centre for Medium-Range Weather Forecasts (ECMWF) reanalysis, HY-2B scatterometer and Soil Moisture Active Passive (SMAP) winds, are used for the assessment. The assessment of the Level 1 observables shows that the instrument's performance and calibration are generally stable. For the assessment of retrieved winds, the general performances of GPS and BDS products are similar. The overall wind speed root-mean-square error is 1.54 m/s for GPS-R and 1.44 m/s for BDS-R when compared with ECMWF, 1.48 m/s for GPS-R and 1.36 m/s for BDS-R when compared with HY-2B, and 2.08 m/s for GPS-R and 2.04 m/s for BDS-R when compared with SMAP. The overall wind speed biases for GPS-R and BDS-R are about zeros when compared with each dataset. The assessment is also made by the dependence on time, signal-to-noise ratio, observable, GNSS block, wind speed, incidence angle, and geography. Overall, the FY-3E GNOS-II global wind product is consistent over time and space with an accuracy meeting the requirement of operational use.**

Index Terms—**Beidou (BDS), FengYun-3E (FY-3E), Global Navigation Satellite System Occultation Sounder II (GNOS-II), Global Navigation Satellite System Reflectometry (GNSS-R), Global Positioning System (GPS), ocean wind, retrieval, validation.**

I. Introduction

THE Global Navigation Satellite System (GNSS) has been proven to be used as signals of opportunity for Earth remote sensing in the configuration of a multistatic radar since 1993 [1]. The major advantage of this technology named GNSS Reflectometry (GNSS-R) is that it uses abundant, free, globally distributed navigation signals so that the receiver can be tiny and cheap without transmitting signals. Ocean surface wind is one geophysical parameter that can be retrieved by GNSS-R. Compared with other conventional instruments that mostly use microwave signals with a higher frequency, GNSS-R uses L-band (with a frequency of ~1.5 GHz) navigation signals that have low attenuation in the presence of rains, which is beneficial for the observation of tropical cyclones [2]. As the development of modern GNSS constellations, including global positioning system (GPS), Beidou (BDS), GLONASS, and Galileo, more signals are now available for the applications of GNSS-R. After a number of coastal and airborne experiments [3], [4], [5], satellite missions including the U.K.-Disaster Monitoring Constellation [6], TechDemoSat-1 [7], Cyclone Global Navigation Satellite System (CYGNSS) [8] and BuFeng-1 A/B [9] have validated the retrieval of ocean surface winds from reflected GNSS signals.

The Global Navigation Satellite System Occultation Sounder II (GNOS-II) onboard the FengYun-3E (FY-3E) satellite launched on July 5, 2021, is a GNSS remote sensor that can collect data from both GNSS radio occultation and GNSS-R [10]. The FY-3E satellite is at an altitude of 836 km in a sun-synchronous orbit (SSO) descending in the early morning at around 6 local solar time (LST) [11]. Some parameters of the orbit and instrument are listed in Table I. Given the sampling frequency of 1 Hz, the spacing of wind samples between one and another on a given track is about 5.6 km. Details of the mission and instrument can also be found in [10].

The first uniqueness of GNOS-II is that it can receive reflected signals from multiple GNSS constellations (GPS and BDS currently, and Galileo soon by sending commands). Second, as GNOS-II is at an orbit of high inclination angle, its wind product can achieve nearly global coverage. Finally, since FY-3E is an operational satellite, its data latency is less than 3 h, which

TABLE I
ORBIT AND INSTRUMENT PARAMETERS OF FY-3E GNOS-II

Altitude	836 km
Inclination angle	98.5°
Number of nadir reflection antenna	1
Number of reflection channels	8 (4 of GPS, 4 of BDS)
Range of incidence angles	0°–55°
GNSS frequency	GPS L1 C/A and BDS B1I
Reflection antenna peak gain	> 14 dBi
Coherent integration time	1 ms
Non-coherent integration times	1000

is applicable for operational use and also applies additional requirements to the retrieval algorithm [10].

Previous studies have shown that the relationship between GNSS-R observable and wind speed differs significantly at low wind speeds and high wind speeds (especially in the tropical cyclone environment) due to differences in the sensitivity to wind speed and also sea state condition [12], [13]. Therefore, two different wind products of GNOS-II are planned to be developed: A global wind product that has the highest accuracy for low-to-medium wind speeds (<25 m/s), which account for more than 99% area over the globe; a cyclone wind product optimized for high wind speeds (up to ∼60 m/s) in the environment of tropical and extratropical cyclones. The global wind product can be used for global applications, such as global data assimilation and climatology studies. The cyclone wind product is mainly aimed for cyclone monitoring, regional data assimilation, and related studies.

This article will present a comprehensive assessment of the GNOS-II global wind product focusing on low-to-medium wind speeds (<25 m/s). The wind products from GPS-R and BDS-R are assessed separately and compared with each other. Note that the differences between GPS-R and BDS-R in spaceborne wind retrieval have never been studied before. One difficulty in validating the retrieved winds of FY-3E GNOS-II is that the satellite is in SSO descending in the early morning so that its product has few collocations with observations from many other polar-orbit satellites that descend at different times. This article will assess the GNOS-II wind product using numerical weather prediction (NWP) model data and satellite observations that lie in the similar orbit of FY-3E.

The rest of this article is organized as follows. Section II gives an overview of the GNOS-II wind speed retrieval algorithm. Section III introduces the GNOS-II data and wind data used for the assessment as well as the collocation method. Section IV presents an assessment on the Level 1 (L1) observables. Section V presents the assessment results on the Level 2 (L2) wind product by comparing them with the NWP model winds and satellite observations. Finally, Section VI concludes this article.

II. OVERVIEW OF THE WIND SPEED RETRIEVAL ALGORITHM

The measurement provided by the GNOS-II instrument is the delay-Doppler map (DDM). In the L1 data processing, the DDMs in raw counts are first calibrated to bistatic radar cross section (BRCS). Observables, the delay-Doppler map average
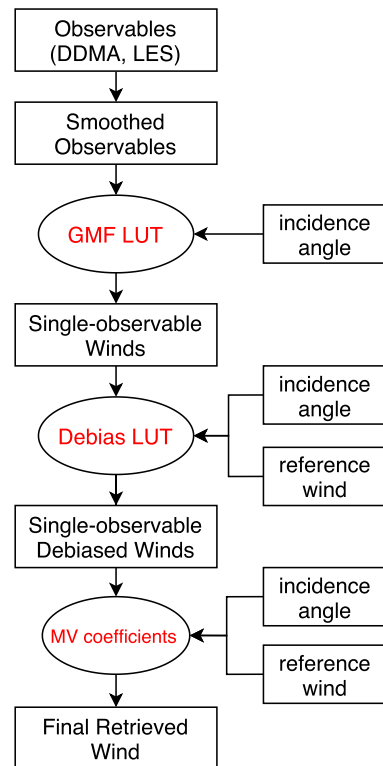

Fig. 1. Flowchart the GNOS-II GNSS-R wind speed retrieval algorithm.

(DDMA) and leading edge slope (LES), are then computed from the DDM BRCS. Details for the L1 processing can be found in [10]. Particularly, the effective isotropic radiated power (EIRP) of GNSS satellites (GPS and BDS) are estimated by static lookup tables (LUTs) constructed from data collected by two power monitors [10].

Fig. 1 shows a flowchart of the GNOS-II L2 global wind speed retrieval algorithm. The observables are first smoothed in time to reduce measurement noise. The number of observables in the smoothing average is limited by the 25-km spatial resolution requirement. Wind speeds retrieved from the DDMA and LES observables are then computed by the geophysical model function (GMF) LUTs, in which the retrieved wind is a function of observable and incidence angle. The winds retrieved from a single observable are later corrected using the debias LUTs in which the bias is a function of reference wind and incidence angle. The final retrieved winds are computed by combining the debiased winds retrieved from DDMA and LES using a minimum variance (MV) estimator [14] where the MV coefficients are a function of reference wind and incidence angle. All LUTs were trained previously using three months of in-orbit data with collocated European Centre for Medium-Range Weather Forecasts (ECMWF) ERA5 reanalysis winds [15]. All LUTs were developed separately for GPS-R and BDS-R. In the real-time retrieval processing, the reference winds in the use of debias LUT and computation of MV coefficients are from the High-Resolution Forecast (HRES) product of the ECMWF operational forecast [16]. The use of ECMWF operational forecast product rather than the reanalysis product in the real-time

processing is to meet the requirement of data latency. Details for the wind speed retrieval algorithm and training of LUTs are described in a companion paper [17].

III. DATA DESCRIPTION AND COLLOCATION METHOD

A. GNOS-II Data

Six months of GNOS-II L2 product from July 10, 2021, to December 31 were used in this study. All data over land and ice were filtered out. Except for the retrieved wind speeds, smoothed Level 1 observables (DDMA and LES) and other metadata [incidence angle and GNSS pseudorandom noise (PRN) code] are also included in the L2 product.

Before assessing the L2 wind product, a quality control (QC) scheme described as follows was first applied to remove data with larger uncertainty.

1) Bit0 of the HDF variable "Sws_quality_flag" in the L2 data is required to be zero. This applies some basic operational QCs to the data. A detailed description of the variable is in the Appendix.
2) GPS-R data with PRN code 10 and 32 were discarded because we found the EIRP of the two satellites has very larger uncertainty.
3) GPS-R data with GPS PRN 22 from November 23 to December 3 were discarded because we found the status of this GPS satellite is unhealthy and its signal is weak during the time.

This QC scheme was applied to data in all the following sections unless particularly specified.

B. NWP Data

ECMWF is a global medium-range NWP model. The 10-m winds of the ECMWF ERA5 reanalysis product [15] are used for the general evaluation of GNOS-II retrieved winds. The ERA5 winds are interpolated at each specular point of GNOS-II linearly in time and space.

C. Scatterometer Winds

Scatterometers have provided accurate satellite observations of ocean surface winds over the last decades. Since both scatterometer and GNSS-R measure the ocean surface roughness, it is important to assess the GNOS-II wind product using scatterometer data. However, as FY-3E is in SSO descending at around 6 LST, it has few collocations with many scatterometers, such as the advanced scatterometer whose orbits descend at times far from 6 LST. In this study, the scatterometer (HSCAT) winds that onboard the Chinese HY-2B satellite are used for the assessment. HY-2B was launched on October 25, 2018. It is operated by the Chinese National Satellite Ocean Application Service. The satellite is in SSO at 970-km altitude with 99.34° inclination descending at 6 LST [18]. Since the descending time of HY-2B and FY-3E is about the same, GNOS-II and HY-2B HSCAT can have a large number of wind collocations. Fig. 2(a) and (b) shows the time of wind observations from GNOS-II and HY-2B on a single day (August 15, 2021).
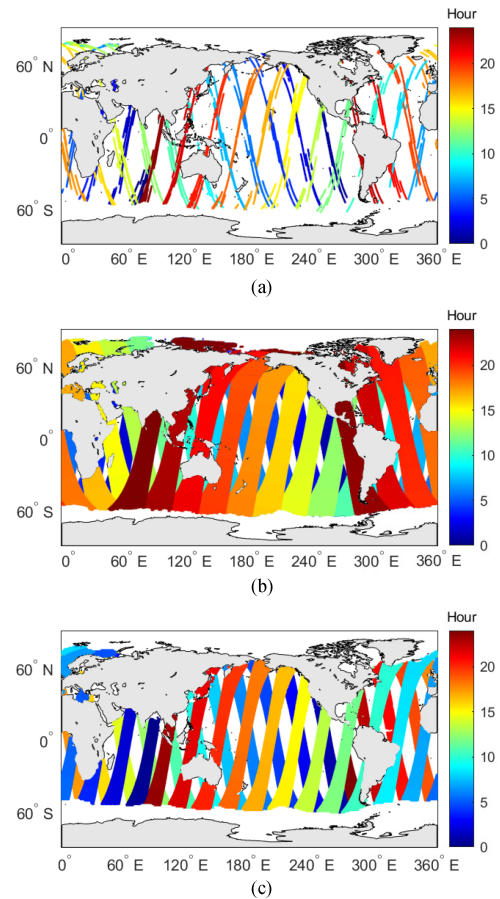

Fig. 2. Time (hour of the day, UTC) of wind obervations for (a) FY-3E GNOS-II, (b) HY-2B scatterometer, and SMAP (c) on August 15, 2021. The three satellites are all in SSO descending at about 6 LST. This figure illustrates the collocations among the three dataset.

HSCAT is a rotating-beam scatterometer operating in Ku-band and can provide 10-m wind observations in a 1300-km swath. The 25-km wind product of HY-2B was used in this study to evaluate the performance of GNOS-II wind product. The accuracy of HY-2B winds is about 1 m/s based on previous studies [18], [19]. The collocation criterion between HY-2B winds and GNOS-II winds is 25-km in space and 1 h in time.

D. Soil Moisture Active Passive (SMAP) Winds

SMAP is a NASA satellite mission launched on January 31, 2015, designed for the observation of soil moisture [20]. It consists of a passive radiometer and a synthetic-aperture radar operating in L-band with multiple polarizations. Other than the baseline science goals, the SMAP L-band radiometer can also retrieve ocean surface winds. Although the global accuracy of SMAP wind product is slightly worse than that of many other spaceborne sensors, it have advantages in the retrieval of high wind speeds: The observed wind-induced surface brightness temperature does not saturate at high winds and the L-band signals are not affected by the rain attenuation [21].

SMAP is in SSO at 685-km, altitude also descending at 6 LST, so it has a large number of collocations with FY3E. The
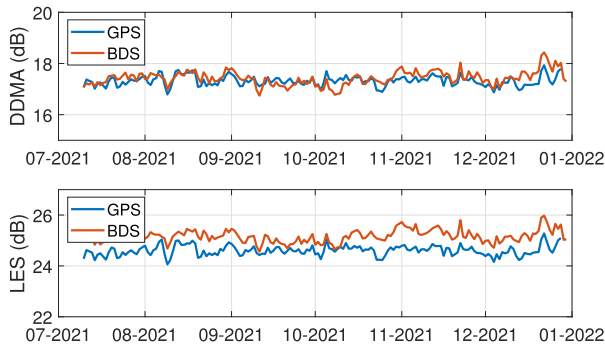
Fig. 3. Time series of the daily-averaged DDMA (top) and LES (bottom) for GPS-R and BDS-R from July 10, 2021, to December 31, 2021.
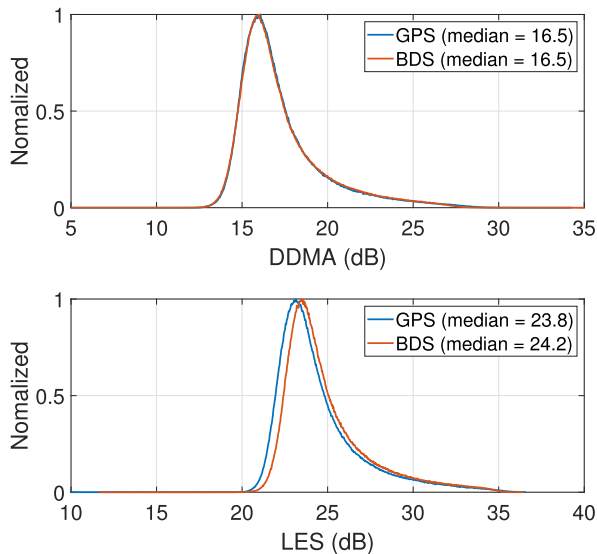

Fig. 4. Histogram of DDMA (top) and LES (bottom) for GPS-R and BDS-R from July 10, 2021, to December 31, 2021.

time of SMAP wind observation on the same day of Fig. 2(a) is shown in Fig. 2(c). The swath of SMAP wind product is around 1000 km. This study uses the SMAP 0.25° gridded wind product provided by the Remote Sensing System.[1] The collocation criterion between SMAP winds and GNOS-II winds is 25-km in space and 1 h in time.

IV. ASSESSMENT OF LEVEL 1 OBSERVABLES

Before assessing the retrieved winds, it is important to first assess the Level 1 observables to evaluate the performance of the instrument and calibration.

Fig. 3 shows the time series of the daily-averaged DDMA and LES for GPS-R and BDS-R. The change of observables is generally less than 0.5 dB, showing that the performance of the instrument and calibration for GPS-R and BDS-R is stable over time. Fig. 4(top) shows the histogram of DDMA and LES for GPS-R and BDS-R. It can be observed that the distributions of DDMA for GPS-R and BDS-R match very well.

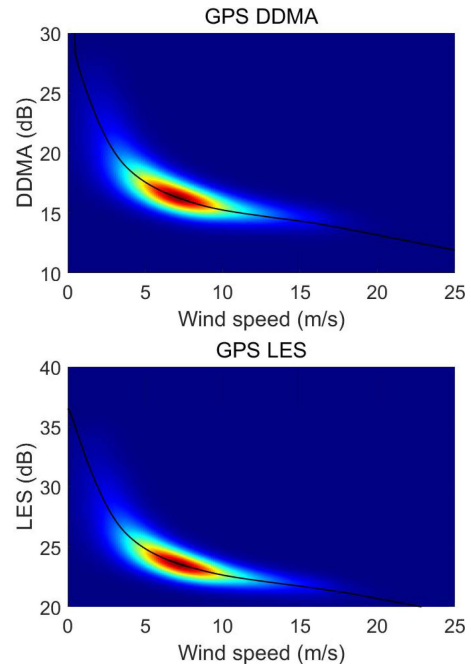[1][Online]. Available: https://www.remss.com/missions/smap/winds/

Fig. 5. Examples of DDMA and LES observables from GPS-R versus corresponding wind speeds at incidence angles 22°–32°, overlaid by the GMF at incidence angle of 27°.

Since DDMA is an average of the NBRCS, which should only be related to the geometry and surface roughness, not the type of constellation, this cross-validates the general power calibration of the instrument for GPS-R and BDS-R. In Fig. 4(bottom), the distributions of LES for GPS and BDS are slightly different. This could result from the difference in the chip length of GPS and BDS signals (293.3 m for GPS and 146.6 m for BDS) while further analysis is required.

Figs. 5 and 6 show the density scatter plots between the observables (DDMA and LES) and collocated ERA5 winds for GPS-R and BDS-R, respectively, for data at incidence angles 22°–32°. The trained GMFs at 27° for both observables are also overlaid on each subfigure (the average incidence angle for all data is about 27°). The GMFs match with the highest density part of the data. Also, the relationships between observables and wind speeds are similar for GPS-R and BDS-R. To compare the observables from GPS and BDS, bin-averaged DDMA and LES at wind speeds from 0 to 25 m/s are shown in Fig. 7. The increment of wind speed is 1 m/s and the bin width is ±1 m/s. The relationships between observables and wind speed for GPS and BDS agree well with each other at 2–20 m/s except a small bias in the LES. The differences at wind speeds below 2 m/s and above 20 m/s are possibly due to lack of data.

To investigate the dependence of observables on the incidence angle, bin-averaged observables at incidence angles from 0° to 53° are shown in Fig. 8. To eliminate the dependence on the wind speed, the wind speeds are restricted in the range of 6–6.5 m/s. The increment of incidence angle is 1° and the bin width is ±1°. The numbers of sample counts for each incidence angle bin are shown on the same figure. Note that the maximum incidence angle for all data is about 53° and the peak receiver antenna gain
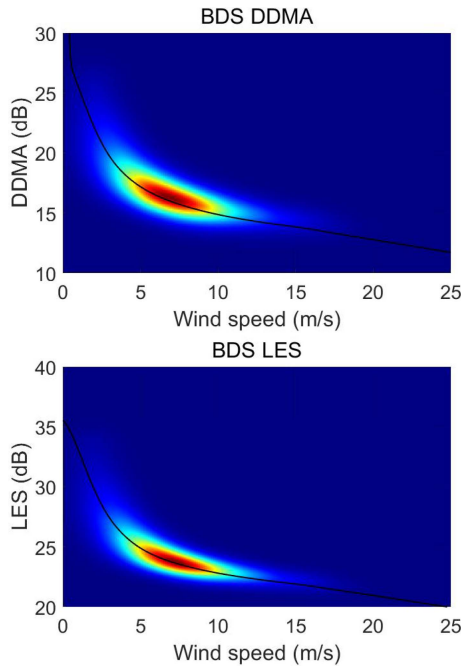
Fig. 6. Examples of DDMA and LES observables from BDS-R versus corresponding wind speeds at incidence angles 22°–32°, overlaid by the GMF at incidence angle of 27°.

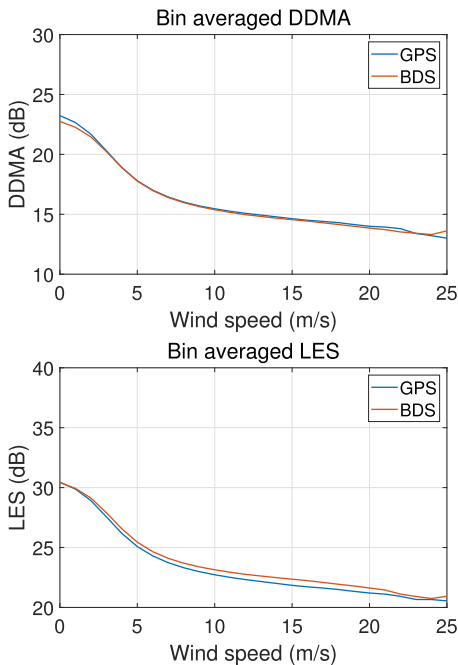Fig. 7. Bin-averaged DDMA and LES from GPS and BDS versus corresponding wind speeds. The bin width is ±1 m/s.
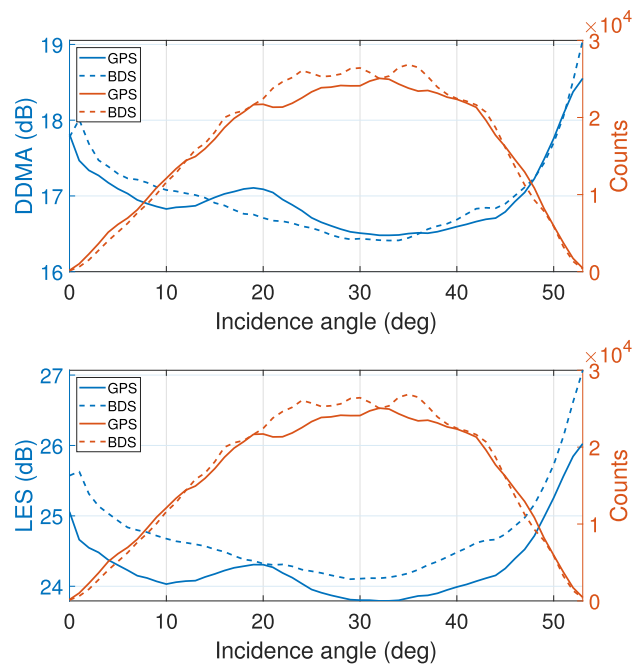

Fig. 8. Bin-averaged observables (DDMA on top and LES on bottom) and number of sample counts for GPS-R and BDS-R at different incidence angles for wind speeds of 6–6.5 m/s. The bin width is ±1°.

to be errors of estimated GPS EIRP from the static LUTs (not shown), which should be corrected in the future.

V. ASSESSMENT OF LEVEL 2 WIND SPEEDS

A. Case Study

We will first present two case studies to show the qualitative performance of GNOS-II L2 wind speeds. Fig. 9 shows a case when GNOS-II wind observations passing the center of Tropical Storm Fred in the Gulf of Mexico on August 15, 2021. Fig. 9(a) shows the GNOS-II wind speed observations from GPS and BDS signals. The collocated ECMWF wind speeds, HY-2B wind speeds, and SMAP wind speeds are shown in Fig. 9(b)–(d), respectively. The time differences between GNOS-II observations and collocated model winds or satellite observations are within 1 h. The storm center reported by the National Hurricane Center best track data is marked on each subfigure as a black hexagram and can be used as a reference to align each subfigure. By comparing Fig. 9(a) and (b), it can be clearly seen that GNOS-II observations match very well with ECMWF model winds and capture most of the structure of the storm. In Fig. 9(c), the HY-2B wind observations have a large swath but miss observations in the center of the storm due to rain contamination and other QC issues. In Fig. 9(d), SMAP wind observations can capture the structure of the storm and are a little higher than the others. However, SMAP wind speeds are a little noisier at low wind speeds than the others. This case also shows that although the GNOS-II global wind product is not optimized specifically for tropical cyclones where the waves are fetch-limited, it can still resolve the structure of some medium-scale tropical storms.

occurs at an incidence angle of 20°. It is clearly seen that both DDMA and LES for GPS-R and BDS-R have some dependence on the incidence angle. In general, the DDMA and LES are larger at low and high incidence angles. This dependence is possibly from some weak assumptions in the Level 1 calibration [22] and should be removed in the wind retrieval algorithm. The little increase of observables at around 20° for GPS-R was found
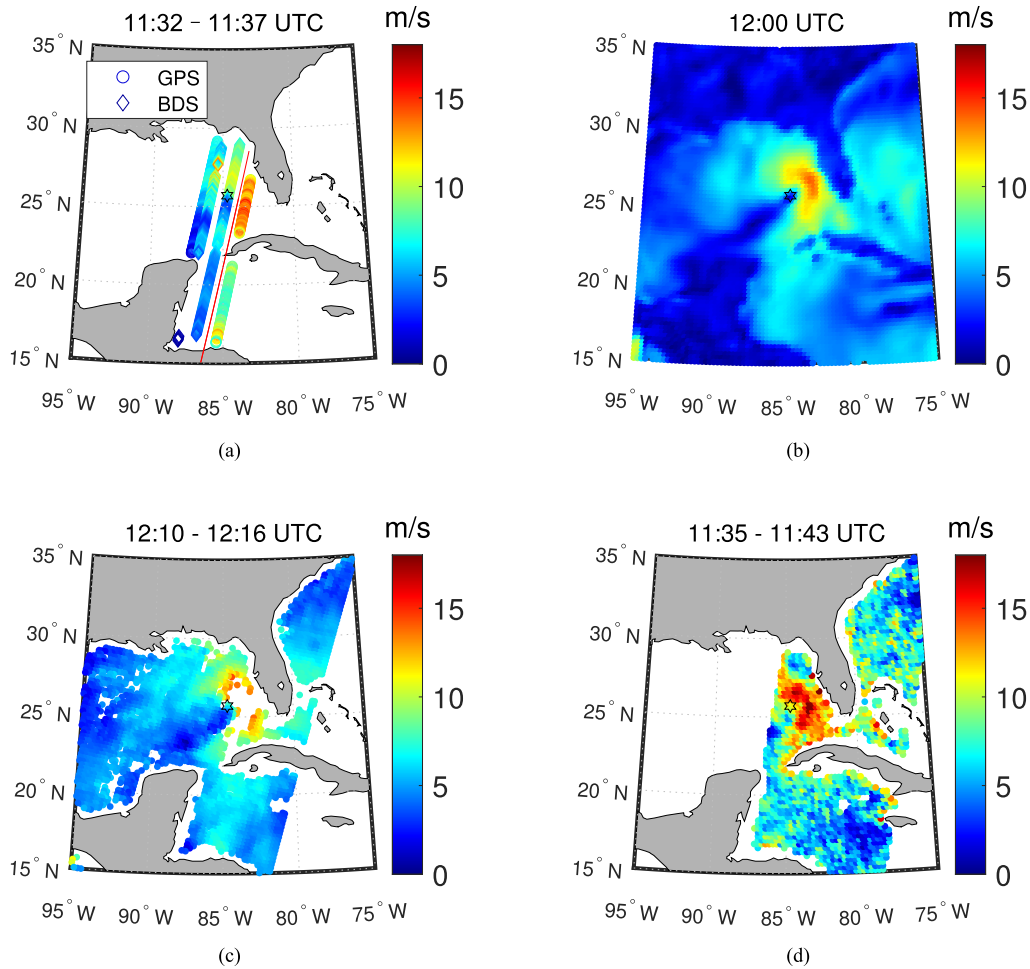
Fig. 9. Case study of GNOS-II wind observations passing the center of Tropical Storm Fred on August 15, 2021. (a) GNOS-II wind speed observations where different marker symbol stands for observations from GPS or BDS signals. The red line stands for the subsatellite points. (b) Collocated ECMWF wind speeds. (c) Collocated HY-2B wind speeds. (d) Collocated SMAP wind speeds. The time of the observation or model is displayed on the title of each subfigure. The storm center reported by the best track data is marked on each subfigure as a black hexagram.

B. Comparison With NWP Model Winds

In this section, the GNOS-II L2 winds are compared with the NWP model winds, i.e., ECMWF ERA5 reanalysis winds.

1) Overall Statistics: Fig. 10 shows the scatter density plots of GNOS-II L2 GPS-R and BDS-R wind speeds against collocated ECMWF wind speeds. The number of collocations, wind speed bias (defined as GNOS-II winds minus model winds), and wind speed root-mean-square error (RMSE) are listed in Fig. 10. They show good agreements between ECMWF and GNOS-II winds for both GPS-R and BDS-R, where most of the data lie along the 1:1 diagonal. The bias is 0.05 m/s for GPS-R and 0.04 m/s for BDS-R. The RMSE is 1.54 m/s for GPS-R and 1.44 m/s for BDS-R.

2) Statistics Over Time: We also assess the wind speed statistics over time. Fig. 11 shows the time series of the daily-averaged wind speed RMSE and bias from July 10, 2021, to December 31, 2021. The overall statistics are stable over time for both GPS-R and BDS-R. For both GPS-R and BDS-R winds, the RMSE is lower than 2 m/s and the bias is close to zero in each day.

3) Statistics Versus SNR: We now assess the wind speed error statistics with respect to the DDM signal-to-noise ratio (SNR). SNR was found to be a good data quality indicator of retrieved winds. The computation of SNR can be found in [10]. Fig. 12 shows the histogram and median of SNR for GPS-R and BDS-R. The median SNR of BDS-R is slightly lower than that of GPS-R because some BDS satellites are in the IGSO orbit. The altitude of IGSO orbit (∼35 000 km) is higher than that of MEO orbit (∼21 000 km) and results in lower SNR. To compute statistics with respect to SNR, the QC on SNR in the L2 HDF variable "Sws_quality_flag" is stopped while all other QCs described in Section III-A are kept. Note that the threshold for SNR in the operational QC scheme is −3 dB. Fig. 13 shows the RMSE and data efficiency rate of GNOS-II L2 winds when different SNR thresholds are used for the additional QC. The data efficiency rate is defined as the number of data after all the QC divided by the number of data without any QC. It can be observed that the wind speed error decreases rapidly when the SNR threshold increases. When the SNR threshold is about −10 dB, which corresponds to about 90% data for GPS-R and 80% data for BDS-R, the overall RMSE is still below 2 m/s. When the SNR
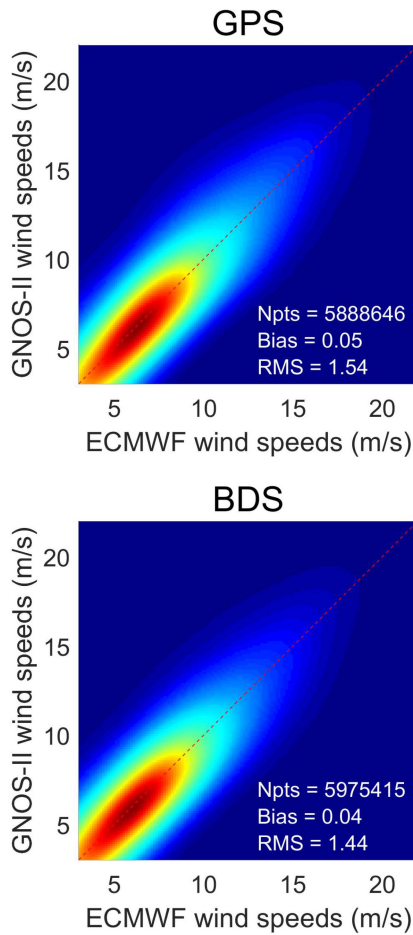
Fig. 10. Scatter density plots of GNOS-II L2 GPS-R (top) and BDS-R (bottom) wind speeds against collocated ECMWF wind speeds. The number of collocations (Npts) and error statistics are reported in each subfigure.
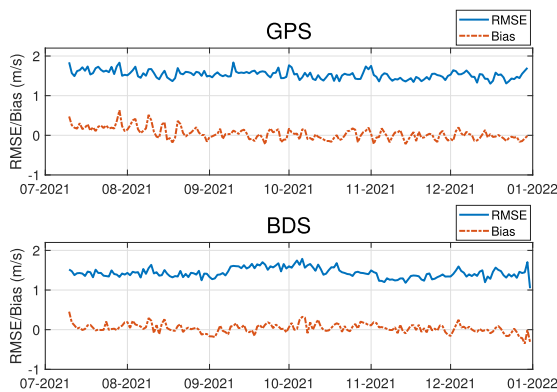

Fig. 11. Time series of the daily-averaged GNOS-II L2 wind speed RMSE and bias from July 10, 2021, to December 31, 2021 (GPS-R on top and BDS-R on bottom).
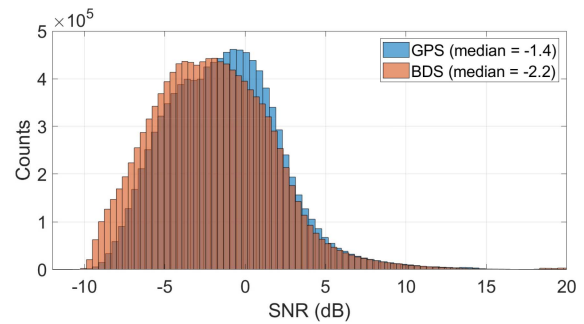

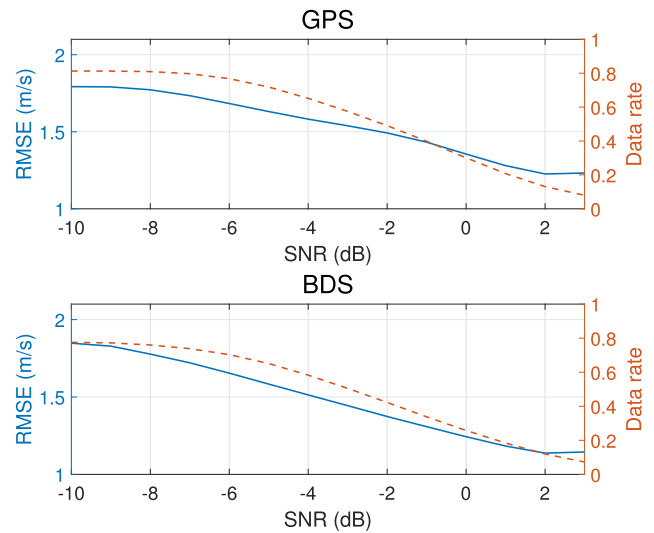Fig. 12. Histogram and median of DDM SNR for GPS-R and BDS-R.

Fig. 13. RMSE and data efficiency rate of GNOS-II L2 winds compared with ECMWF when different SNR thresholds are used for QC (GPS-R on top and BDS-R on bottom).

TABLE II
STATISTICS OF WIND SPEEDS RETRIEVED FROM DDMA, LES, AND MV ESTIMATE FOR GPS-R AND BDS-R

	GPS			BDS		
	DDMA	LES	MV	DDMA	LES	MV
Bias (m/s)	−0.05	0.12	0.05	−0.05	0.08	0.04
RMSE (m/s)	1.58	1.62	1.54	1.54	1.49	1.44

4) Dependence on Observables: Here, we assess the retrieval accuracies of different observables. The bias and RMSE for wind speed retrieved from DDMA, LES, and MV estimate (final retrieval) for GPS-R and BDS-R are listed in Table II. Both DDMA and LES have good retrieval performance. The overall retrieval accuracies of DDMA and LES are similar. In addition, the accuracy of the MV estimate is slightly better than that of any observable proving that the MV estimate can improve the retrieval accuracy by combining the two observables.

5) Dependence on GNSS Block: GNSS satellite blocks are the various generations of satellites for a specific navigation system. GNSS satellites from different blocks can have different performances in reflectometry since they have different orbits and characteristics of transmitted EIRP. In this section, we assess the wind speed error statistics of different GNSS blocks. GPS

threshold is −3 dB, the data efficiency rate is about 60% for GPS-R and 50% for BDS-R. In this case, many data with low SNR are discarded. Note that GNOS-II is at a relatively high altitude and has only one nadir antenna with eight reflection channels for GPS and BDS signals. In order to collect enough scientific data, some data with specular points outside the main beam of the nadir antenna are received.
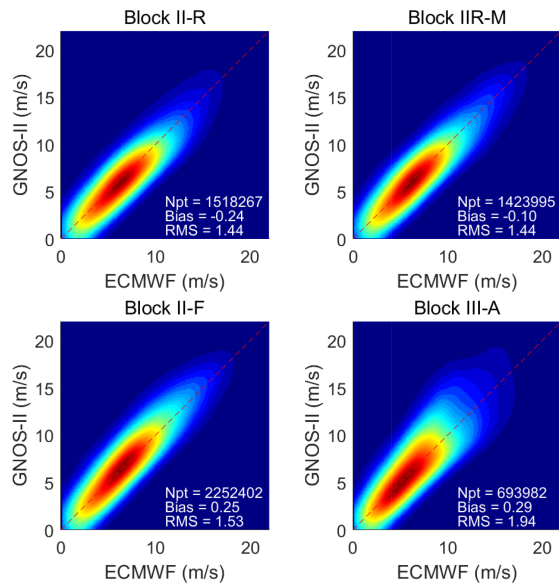
Fig. 14. Scatter density plots of GNOS-II L2 GPS-R and BDS-R wind speeds against collocated ECMWF wind speeds for different GPS blocks.
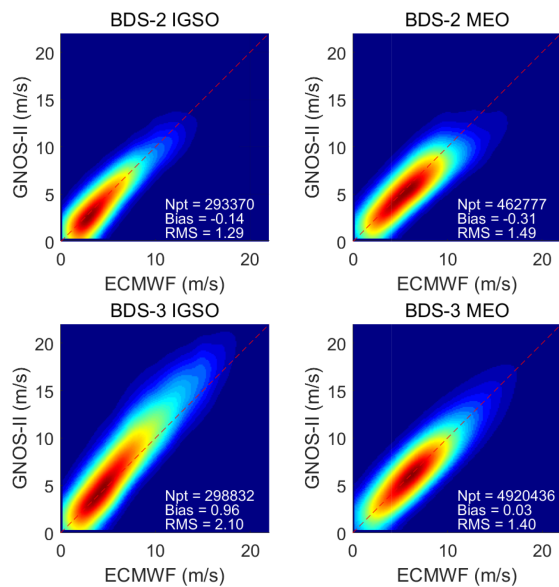

Fig. 15. Scatter density plots of GNOS-II L2 BDS-R and BDS-R wind speeds against collocated ECMWF wind speeds for different BDS blocks.

satellites have four blocks, including Block II-R, Block IIR-M, Block II-F, and Block III-A. BDS satellites also have four blocks, including BDS-2 IGSO, BDS-2 MEO, BDS-3 IGSO, and BDS-3 MEO (GNOS-II does not receive signals of BDS GEO satellites). The scatter density plots and error statistics of different blocks from GPS and BDS are shown in Figs. 14 and 15. Obvious differences in the performance of different blocks for both GPS-R and BDS-R can be observed. For GPS, Block II-R and Block IIR-M have the best results with an RMSE of 1.44 m/s. The data of Block III-A are much more scattered than the others with an RMSE of 1.94 m/s. As the GNSS EIRPs are estimated by static LUTs for GNOS-II [10], the uncertainty of data from GPS satellites (Block III-A especially, and some from
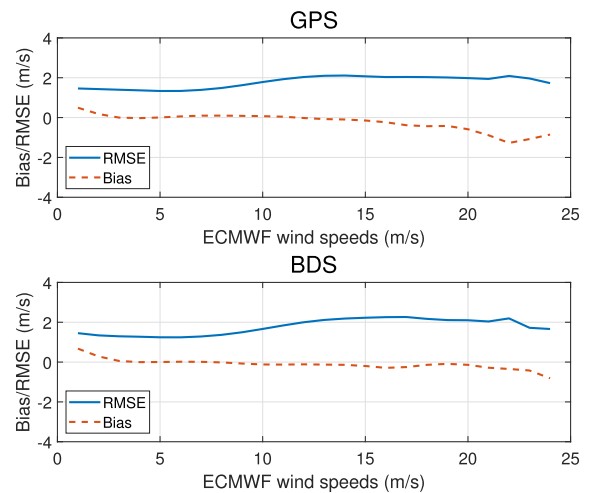

Fig. 16. Error statistics of GNOS-II L2 wind speeds at different ECMWF wind speeds (GPS-R on top and BDS-R on bottom). Those values are computed at a wind speed bin width of ± 1 m/s.

Block IIR-M and II-F) is possibly due to the large variation of the transmitter EIRP over time and region, such as from the flex power event [23]. For BDS, over 80% of the data are from BDS-3 MEO satellites whose RMSE is 1.40 m/s. The bias and error of BDS-3 IGSO are much larger than the others implying that there are some calibration errors with it possibly due to the estimation of EIRP.

6) Dependence on Wind Speed: The error statistics of GNOS-II L2 wind speeds with respect to collocated ECMWF wind speeds are shown in Fig. 16. The results are computed for wind speed from 0 to 24 m/s at a bin width of ± 1 m/s. In general, the bias and RMSE increase as the ECMWF wind speed increases from 3 m/s. For both GPS-R and BDS-R, the bias remains close to zero within 3–20 m/s while RMSE remains lower than 2 m/s within 3–12 m/s and around 2 m/s within 12–20 m/s. The drift of bias at round $20°$ for GPS-R is due to errors of estimated GPS EIRP, as described in Section IV. Small positive bias at low winds under 3 m/s and small negative bias at high winds above 20 m/s can be observed for both GPS-R and BDS-R. This is due to the representation error of the GMFs for the GNOS-II global wind product. Since the GMFs were optimized to achieve the best retrieval accuracy globally when most (more than 90%) of the global wind speeds are within 3–15 m/s, the accuracy of the GMFs decreases slightly at lower and higher wind speeds. Furthermore, the debias LUTs described in Section II should still be improved to correct this wind-dependent bias.

7) Dependence on Incidence Angle: In Section IV, we have shown that the L1 observables have a dependence on the incidence angle due to some calibration issues. Also, as described in Section II, all GMFs and debias LUTs are developed as functions of incidence angle to remove this geometry dependence. So, it is necessary to assess if the retrieved winds still have any dependence on the incidence angle. Fig. 17 shows the average error statistics of GNOS-II L2 wind speeds at different incidence angles at a bin width of $\pm 1°$. The statistics are computed up to $45°$ because the number of data at incidence angle larger
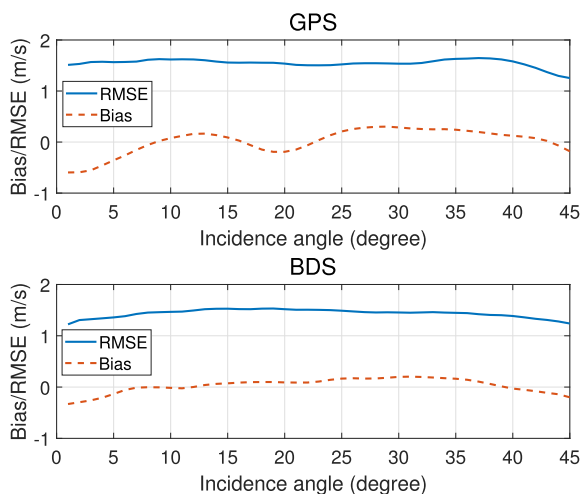
Fig. 17. Error statistics of GNOS-II L2 wind speeds at different incidence angles (GPS-R on top and BDS-R on bottom). Those values are computed at an incidence angle bin width of $\pm 1°$.
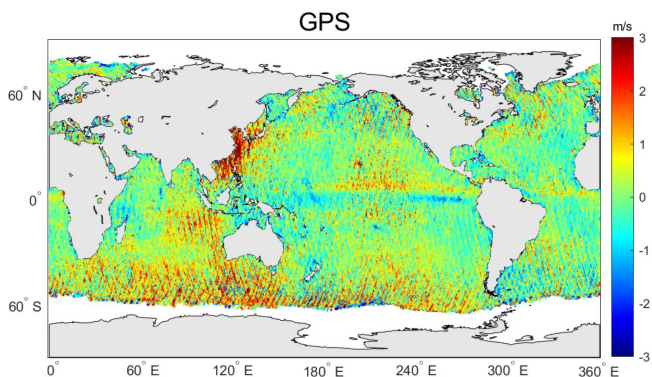

Fig. 18. Global distribution of GNOS-II GPS-R wind speed errors (GNOS-II minus ECMWF) by a $0.5°$ grid size. The errors are averaged in each grid.

Fig. 19. Global distribution of GNOS-II BDS-R wind speed errors (GNOS-II minus ECMWF) by a $0.5°$ grid size. The errors are averaged in each grid.

than 45° are not statistically significant. The dependence on the incidence angle of retrieved winds is now much less than that of the observables compared with Fig. 8. This demonstrates that the wind retrieval process has successfully removed most of the dependences on geometry, although a small bias still remains at very low incidence angle.

8) Dependence on Geography: As GNOS-II can provide wind speeds over the globe, we now assess the global distribution of the wind speed errors. The global map was first gridded by a $0.5°$ grid size. The wind speed errors (GNOS-II minus ECMWF) in each grid are then averaged to generate the global map of wind speed errors. Figs. 18 and 19 show the global maps of wind speed errors for GPS-R and BDS-R, respectively. The maps are not quite smooth as only six months data are used in this study. Overall, the global distributions of wind speed errors for GPS-R and BDS-R are similar. The bias is generally small for most areas of the open ocean. Strong positive biases can be observed in the coastal area of southeastern Asian for both GNSS systems but stronger for GPS. Note that similar patterns can also be observed from CYGNSS data [24]. After an intensive investigation, we found that this was caused by a radio frequency interference and
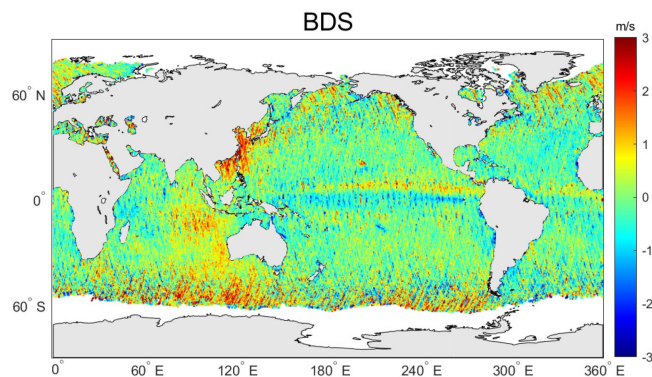
should be corrected in the future. Small positive and negative bias stripes can be found near the equator. The reason could be that ECMWF model winds are less accurate for the region of Inter Tropical Convergence Zone (ITCZ) because of tropical convection and precipitation activities. Large errors can also be observed at high latitudes in the southern hemisphere. This is due to the high wind speeds of extratropical cyclones in the subpolar Westerlies, where the retrieval accuracy decreases. The bias in the north west of Australia within the Indian ocean is still under investigation.

C. Comparison With Satellite Observations

1) Comparison With Scatterometer Winds: In this section, GNOS-II winds are compared with HY-2B scatterometer winds. As HY-2B is also in early-morning SSO orbit, a large number of collocations can be found between GNOS-II and HY-2B winds. As HY-2B is less accurate for wind speed under 3 m/s, the comparison results were computed for wind speeds above 3 m/s. Fig. 20 shows the scatter density plots of GNOS-II L2 GPS-R and BDS-R wind speeds against collocated HY-2B wind speeds. GNOS-II winds show good agreements with HY-2B winds both in GPS-R and BDS-R. The biases are almost zero with −0.07 m/s for GPS-R and −0.09 m/s for BDS-R. The RMSE is 1.48 m/s for GPS-R and 1.36 m/s for BDS-R, where the "error" is defined as GNOS-II minus HY-2B wind speeds. The statistics compared with HY-2B are a little better than those compared with ECMWF. The possible reason is that GNOS-II GNSS-R winds and HY-2B scatterometer winds, both as satellite observations, have more similar spatio-temporal representation and measure the equivalent neutral winds [25]. The error statistics of GNOS-II L2 wind speeds at different HY-2B wind speeds are shown in Fig. 21 at a bin width of ± 1 m/s. The results are similar to ones compared with ECMWF. The bias remains close to zero for wind speed up to ~15 m/s and slightly decreases as HY-2B wind speed increases.

The geographical distribution of GNOS-II errors compared with HY-2B winds is also similar to that compared with ECMWF, as shown Figs. 18 and 19, and thus not shown here. The only difference is that GNOS-II winds match well with HY-2B winds in the region of ITCZ, which implies that satellite
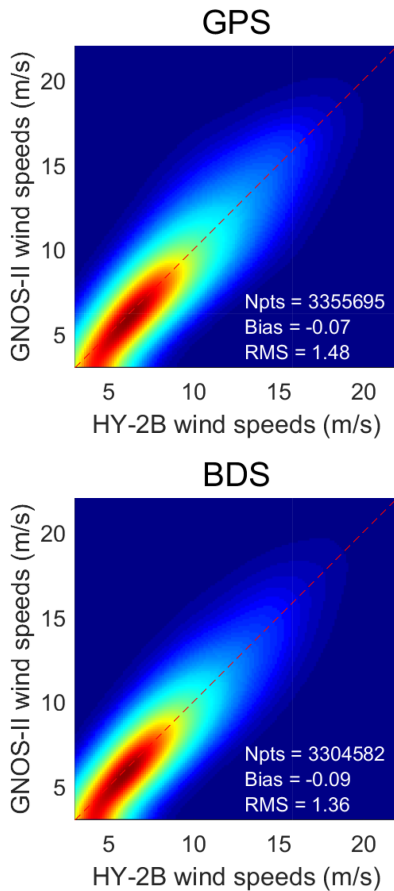
Fig. 20. Scatter density plots of GNOS-II L2 GPS-R (top) and BDS-R (bottom) wind speeds against collocated HY−2B scatterometer wind speeds.
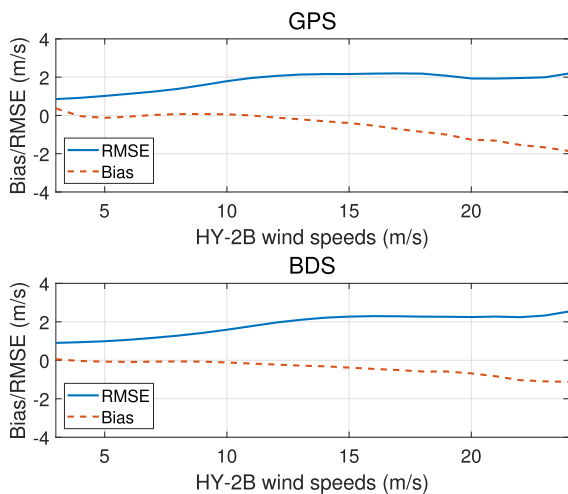

Fig. 21. Error statistics of GNOS-II L2 wind speeds at different HY-2B wind speeds (GPS-R on top and BDS-R on bottom). Those values are computed at wind speed bin width of ±1 m/s.

observations are generally more accurate than NWP models for ITCZ.

2) Comparison With SMAP Winds: In this section, GNOS-II winds are compared with SMAP winds. A large number of collocations can be found between GNOS-II and SMAP winds as both are in the early-morning SSO orbit. Fig. 22 shows the scatter
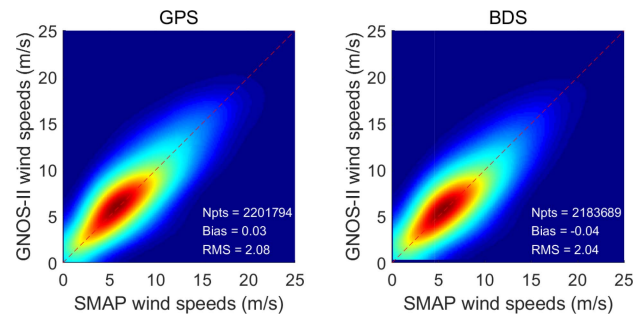

Fig. 22. Scatter density plots of GNOS-II L2 GPS-R (top) and BDS-R (bottom) wind speeds against collocated SMAP wind speeds.
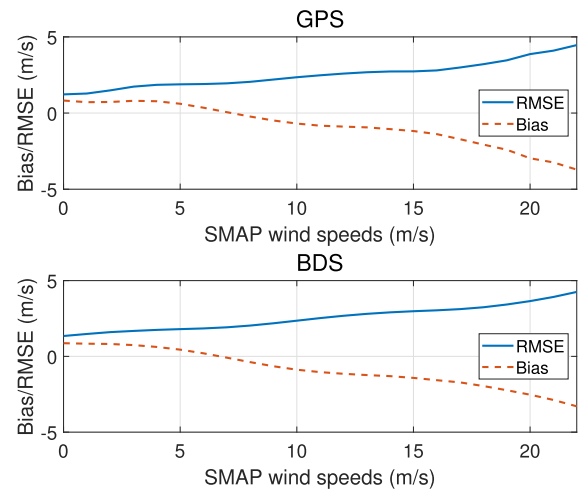
Fig. 23. Error statistics of GNOS-II L2 wind speeds at different SMAP wind speeds (GPS-R on top and BDS-R on bottom). Those values are computed at a wind speed bin width of ±1 m/s.

density plots of GNOS-II L2 GPS-R and BDS-R wind speeds against collocated SMAP wind speeds. The comparison was made for wind speeds under 25 m/s as this article focuses on assessing low-to-medium wind speeds. GNOS-II winds generally agree with SMAP winds with RMSE about 2 m/s and bias about 0 m/s when the "error" is defined as GNOS-II minus SMAP wind speeds. The RMSE compared with SMAP is higher than compared with ECMWF or HY-2B, because SMAP wind speeds are noisier at low wind speeds and also along coastlines [24]. The error statistics of GNOS-II L2 wind speeds at different SMAP wind speeds are shown in Fig. 23 at a bin width of ±1 m/s. The bias (GNOS-II minus SMAP) is slightly positive at wind speeds below 7 m/s and decreases when wind speed increases. This result is expected as the current GMFs of the GNOS-II wind product were trained from collocated ECMWF winds, which are generally lower than SMAP winds at high wind speeds. GMFs of high wind speeds for GNOS-II should be trained in the future to achieve good performance at high wind speeds.

D. Error Correlation Analysis

In Section II, we have mentioned that the retrieval process has used ECMWF operational forecasts for the wind speed debias. It is important to note that the bias is not computed directly, but

Fig. 24. Scatter density plots between the errors of GNOS-II (left-hand side for GPS-R, right-hand side for BDS-R) and colloca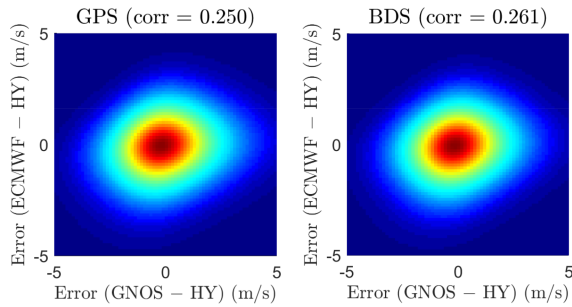ted ECMWF winds when HY-2B winds are used as the reference. The correlation coefficients of the errors are shown on the title of each subfigure.
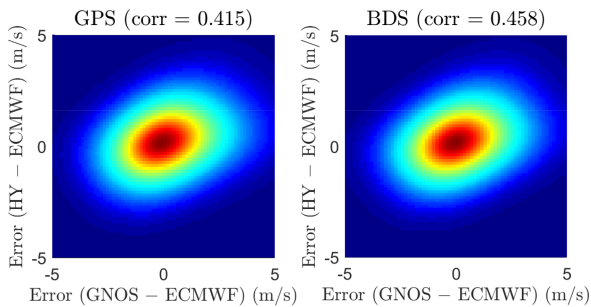

Fig. 25. Scatter density plots between the errors of GNOS-II (left-hand side for GPS-R, right-hand side for BDS-R) and collocated HY-2B winds when ECMWF winds are used as the reference. The correlation coefficients of the errors are shown on the title of each subfigure.

indirectly through empirical LUTs. One concern is that the retrieved winds may have some correlations with ECMWF winds and cannot be "independent" observations, which is harmful to the use in the NWP data assimilation. For example, if they were correlated, the retrieved winds would have a similar bias when the ECMWF wind had a bias for a certain time or region.

To study this correlation, we need a third dataset as the reference and a triple collocation among them [26]. In this section, we use the HY-2B scatterometer wind product as the reference as its wind observations are usually more accurate than NWP model winds [27]. A triple collocation for GNOS-II winds, ECMWF ERA5 winds and HY-2B winds was made. Although the ECMWF ERA5 reanalysis is a little different from its operational model used in the retrieval, they should have very similar error characteristics. Fig. 24 shows the scatter density plots between the errors of GNOS-II and collocated ECMWF winds when HY-2B winds are used as the reference. No obvious correlations are observed from the figures. The Pearson correlation coefficients between the errors of GNOS-II and ECMWF are 0.247 for GPS-R and 0.253 for BDS-R. With these low values of correlation coefficients, the correlation between errors from GNOS-II winds and ECMWF winds can be regarded as negligible. Therefore, it is safe to assume that using ECMWF operational forecast winds in the retrieval process does not introduce error correlations to the wind retrievals.

In an additional check, we also study the correlation between the errors of GNOS-II and HY-2B winds when ECMWF ERA5

winds are used as the reference. Fig. 25 shows the scatter density plots between the errors of GNOS-II and collocated HY-2B winds when ECMWF winds are used as the reference. The correlation coefficients between errors of GNOS-II and HY-2B are 0.409 for GPS-R and 0.448 for BDS-R, which are larger than those between GNOS-II and ECWMF while no HY-2B information is used in the GNOS-II wind retrieval. The reason could be that GNOS-II winds have closer spatio-temporal representation to HY-2 scatterometer winds than NWP model winds as both GNSS-R instrument and scatterometer measure the instantaneous ocean surface roughness.

VI. CONCLUSION

This article presents the first comprehensive assessment of the FY-3E GNOS-II GNSS-R global wind product using its first six months of data. As the retrieval model of this product is optimized using collocated ECMWF winds, the assessment is focused on low-to-medium wind speeds (<25 m/s). As FY-3E is in an SSO descending in the early-morning, ECMWF reanalysis model winds and wind observations from satellites in a similar orbit (HY-2B scatterometer and SMAP) are used for the assessment. Wind products from GPS-R and BDS-R are analyzed separately.

The L1 observables, including the DDMA and LES, are first assessed. The time series of observables show that the performance of the instrument and calibration are stable over time. The distribution of observables shows that the DDMA characteristics are almost the same for GPS-R and BDS-R while LES is a little different possibly due to the difference in the signal chipping length of the two GNSS systems. It is also found that both observables have a strong dependence on the incidence angle, which should be corrected in the L2 processing.

For the assessment on the L2 wind product, the performances of GPS-R and BDS-R winds are generally quite similar. In comparison with the ECMWF model winds, the overall RMSE is 1.54 m/s for GPS-R and 1.44 for BDS-R with both biases close to zero for the six months of data. For the time series of errors, the RMSE remains below to 2 m/s for each day. For errors depending on the DDM SNR, both the RMSE and data efficiency rate decrease when the SNR threshold in the QC is increased. When the SNR threshold is at its operational value, -3 dB, the data efficiency rate is about 60% for GPS-R and 50% for BDS-R. The error statistics are also computed by different GNSS blocks. Noticeable differences in the performance of different blocks for both GPS-R and BDS-R can be observed. The worst retrieval performance is observed from Block III-A from GPS-R and BDS-3 IGSO from BDS-R. This implies that the uncertainty of GNSS transmitted EIRP is one of the major error sources in the wind retrieval. When error statistics are computed at different ECMWF wind speeds, the RMSE remains below or around 2 m/s, and the bias remains near 0 m/s under 20 m/s. When error statistics are computed at different incidence angles, the RMSE and bias remain stable at different incidence angles except for small bias at low incidence angles. This shows that most of the dependences on the geometry of observables from L1 processing have been corrected in the L2 processing. For the

global distribution of wind speed errors, major biases appear in the coastal area of southeastern Asia for both GPS-R and BDS-R, which are caused by a radio frequency interference.

In comparison with the satellite wind observations, the overall RMSE is 1.48 m/s for GPS-R and 1.36 m/s for BDS-R when compared with HY-2B scatterometer winds, 2.08 m/s for GPS-R, and 2.04 m/s for BDS-R when compared with SMAP winds. The overall bias is close to zero when compared with each dataset. When the error statistics are computed at different wind speeds of the reference data, the GNOS-II wind speeds are slightly lower than the reference winds above 15 m/s especially when compared with SMAP winds. These results are expected as SMAP is capable of resolving higher wind speeds than ECMWF, which is used to train the GNOS-II global wind product. The error correlations between GNOS-II winds and ECMWF winds are assessed using a triple collocation among GNOS-II, ECMWF, and HY-2B winds. The error correlations between GNOS-II winds and ECMWF winds are found to be minor, demonstrating that it is currently safe to use ECMWF operational forecasts in the retrieval process.

Several improvements on the GNOS-II wind retrieval scheme will be made in the future. First, the L1 calibration will be improved especially to reduce the geography-dependent bias. Second, more robust GMFs will be trained using more in-orbit data. Third, the EIRP estimations for GPS and BDS transmitters should be improved. A trackwise bias correction method can also be considered to reduce the EIRP estimation errors [24]. Finally, as mentioned before, the global wind product presented in this article is optimized for global low-to-medium wind speeds. In the future, a cyclone wind product whose GMFs are trained for high wind speeds (up to ∼60 m/s) will be developed and assessed using high-wind datasets, such as SMAP and Hurricane Weather Research and Forecasting model.

APPENDIX

Table III shows the detailed description of the HDF variable "Sws_quality_flag" in the GNOS-II L2 product.

TABLE III
GNOS-II L2 VARIABLE "SWS_QUALITY_FLAG" DESCRIPTION

bit0	Overall wind quality, a combination of bit 1, 2, 4, 6, 7, 8, 9, 10
bit1	The retrieved wind speed is negative
bit2	The retrieved wind speed is too high
bit3	The total corrected gain is less than the threshold
bit4	The GNSS transmitter EIRP is less well known
bit5	Model forecast wind is not used
bit6	The retrieved wind speed is filled value
bit7	The number of DDMs in the smoothing is less than 3
bit8	The number of observable used for retrieval is less than 2
bit9	The difference between the NBRCS wind and LES wind is larger than the threshold
bit10	The DDM SNR is smaller than −3 dB

ACKNOWLEDGMENT

REFERENCES

[1] M. Martin-Neira, "A passive reflectometry and interferometry system (PARIS): Application to ocean altimetry," *ESA J.*, vol. 17, no. 4, pp. 331–355, 1993.

[2] V. U. Zavorotny, S. Gleason, E. Cardellach, and A. Camps, "Tutorial on remote sensing using GNSS bistatic radar of opportunity," *IEEE Geosci. Remote Sens. Mag.*, vol. 2, no. 4, pp. 8–45, Dec. 2014.

[3] F. Soulat, M. Caparrini, O. Germain, P. Lopez-Dekker, M. Taani, and G. Ruffini, "Sea state monitoring using coastal GNSS-R," *Geophysical Res. Lett.*, vol. 31, no. 21, 2004, Art. no. L21303.

[4] S. J. Katzberg, O. Torres, and G. Ganoe, "Calibration of reflected GPS for tropical storm wind speed retrievals," *Geophysical Res. Lett.*, vol. 33, no. 18, 2006, Art. no. L18602.

[5] N. Rodriguez-Alvarez, D. M. Akos, V. U. Zavorotny, J. A. Smith, A. Camps, and C. W. Fairall, "Airborne GNSS-R wind retrievals using delay–Doppler maps," *IEEE Trans. Geosci. Remote Sens.*, vol. 51, no. 1, pp. 626–641, Jan. 2013.

[6] M. Clarizia, C. Gommenginger, S. Gleason, M. Srokosz, C. Galdi, and M. D. Bisceglie, "Analysis of GNSS-R delay-Doppler maps from the U.K.-DMC satellite over the ocean," *Geophysical Res. Lett.*, vol. 36, no. 2, 2009, Art. no. L02608.

[7] G. Foti et al., "Spaceborne GNSS reflectometry for ocean winds: First results from the U.K. TechDemoSat-1 mission," *Geophysical Res. Lett.*, vol. 42, no. 13, pp. 5435–5441, 2015.

[8] C. S. Ruf et al., "A new paradigm in earth environmental monitoring with the CYGNSS small satellite constellation," *Sci. Rep.*, vol. 8, no. 1, pp. 1–13, 2018.

[9] C. Jing, X. Niu, C. Duan, F. Lu, G. Di, and X. Yang, "Sea surface wind speed retrieval from the first Chinese GNSS-R mission: Technique and preliminary results," *Remote Sens.*, vol. 11, no. 24, 2019, Art. no. 3013.

[10] G. Yang et al., "FY3E GNOS II GNSS reflectometry: Mission review and first results," *Remote Sens.*, vol. 14, no. 4, 2022, Art. no. 988. [Online]. Available: https://www.mdpi.com/2072-4292/14/4/988

[11] P. Zhang et al., "FY-3E: The first operational meteorological satellite mission in an early morning orbit," *Adv. Atmosph. Sci.*, vol. 39, pp. 1–8, 2022.

[12] C. S. Ruf and R. Balasubramaniam, "Development of the CYGNSS geophysical model function for wind speed," *IEEE J. Sel. Topics Appl. Earth Observ. Remote Sens.*, vol. 12, no. 1, pp. 66–77, Jan. 2019.

[13] M. P. Clarizia and C. S. Ruf, "Statistical derivation of wind speeds from CYGNSS data," *IEEE Trans. Geosci. Remote Sens.*, vol. 58, no. 6, pp. 3955–3964, Jun. 2020.

[14] M. P. Clarizia, C. S. Ruf, P. Jales, and C. Gommenginger, "Spaceborne GNSS-R minimum variance wind speed estimator," *IEEE Trans. Geosci. Remote Sens.*, vol. 52, no. 11, pp. 6829–6843, Nov. 2014.

[15] H. Hersbach et al., "The ERA5 global reanalysis," *Quart. J. Roy. Meteorological Soc.*, vol. 146, no. 730, pp. 1999–2049, 2020.

[16] R. Owens and T. Hewson, *ECMWF Forecast User Guide*. Reading, U.K.:ECMWF, 2018.

[17] J. Xia et al., "The FY3E GNOS II GNSS reflectometry: Calibration and wind speed retrieval," *IEEE J. Sel. Topics Appl. Earth Observ. Remote Sens.*, to be published.

[18] H. Wang, J. Zhu, M. Lin, Y. Zhang, and Y. Chang, "Evaluating chinese HY-2B HSCAT ocean wind products using buoys and other scatterometers," *IEEE Geosci. Remote Sens. Lett.*, vol. 17, no. 6, pp. 923–927, Jun. 2020.

[19] Z. Wang et al., "Validation of new sea surface wind products from scatterometers onboard the HY-2B and MetOp-C satellites," *IEEE Trans. Geosci. Remote Sens.*, vol. 58, no. 6, pp. 4387–4394, Jun. 2020.

[20] D. Entekhabi et al., "The soil moisture active passive (SMAP) mission," *Proc. IEEE*, vol. 98, no. 5, pp. 704–716, May 2010.

[21] T. Meissner, L. Ricciardulli, and F. J. Wentz, "Capability of the SMAP mission to measure ocean surface winds in storms," *Bull. Amer. Meteorological Soc.*, vol. 98, no. 8, pp. 1660–1677, 2017.

[22] M. P. Clarizia and C. S. Ruf, "Wind speed retrieval algorithm for the cyclone global navigation satellite system (CYGNSS) mission," *IEEE Trans. Geosci. Remote Sens.*, vol. 54, no. 8, pp. 4419–4432, Aug. 2016.

[23] P. Steigenberger, S. Thölert, and O. Montenbruck, "Flex power on GPS block IIR-M and IIF," *GPS Solutions*, vol. 23, no. 1, pp. 1–12, 2019.

[24] F. Saïd, Z. Jelenak, J. Park, and P. S. Chang, "The NOAA track-wise wind retrieval algorithm and product assessment for CyGNSS," *IEEE Trans. Geosci. Remote Sens.*, vol. 60, Jul. 2022, Art. no. 4202524.

[25] J. de Kloe, A. Stoffelen, and A. Verhoef, "Improved use of scatterometer measurements by using stress-equivalent reference winds," *IEEE J. Sel. Topics Appl. Earth Observ. Remote Sens.*, vol. 10, no. 5, pp. 2340–2347, May 2017.

[26] D. Pascual, M. P. Clarizia, and C. S. Ruf, "Improved CYGNSS wind speed retrieval using significant wave height correction," *Remote Sens.*, vol. 13, no. 21, 2021, Art. no. 4313.

[27] A. Verhoef, J. Vogelzang, and A. Stoffelen, "Scienfitic validation report (SVR) for the HY-2 winds," EUMETSAT OSI SAF, Lannion cedex, France, Tech. Rep. SAF/OSI/CDOP3/KNMI/TEC/RP/393, 2021.

Na Xu received the B.S. degree in atmospheric science from the Ocean University of China, Qingdao, China, in 2005, and the Ph.D. degree in atmospheric physics and environment from the Institute of Atmospheric Physics, Chinese Academy of Sciences, Beijing, China, in 2010.

She is currently a Professor with the National Satellite and Meteorological Center, China Meteorological Administration, Beijing, China. She is the Instrument Scientist of the Medium Resolution Spectral Imager onboard the Chinese FengYun-3D (FY-3D), in charge of the calibration and validation for MERSI II, and the Chief Director of the product generation system (PGS) for FengYun-3 and FengYun-4 Projects. Her research interests include calibration and validation for optical sensors, and remote sensing of cloud microphysics.

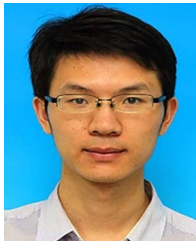Dr. Xu was a Member of the Global Space-Based Inter-Calibration System (GSICS/WMO).

Feixiong Huang (Member, IEEE) received the B.S. degree in geodesy and geomatics engineering from Wuhan University, Wuhan, China, in 2014, and the Ph.D. degree in aeronautical and astronautical engineering from Purdue University, West Lafayette, IN, USA, in 2020.

He was a Visiting Scientist with the Royal Netherlands Meteorological Institute, DeBilt, The Netherlands, in Summer 2019 with funding from the EUMETSAT OSI SAF Visiting Scientist Program. He is currently a Postdoctoral Researcher with the National Space Science Center, Chinese Academy of Sciences, Beijing, China. His research interests include spaceborne GNSS-R, microwave ocean remote sensing, and atmospheric data assimilation.

Guanglin Yang received the M.S. degree in atmosphere physics from Peking University, Beijing, China, in 2002.

He is currently a Senior Engineer in ionosphere observation with the National Center for Space Weather, China Meterological Administration, Beijing, China. His research interests include GNSS radio occultation, GNSS/MET and coupling of upper atmosphere and ionosphere.

Junming Xia received the B.S. degree in physics from the Changsha University of Science and Technology, Changsha, China, in 2009 and the M.S. and Ph.D. degrees in earth and space exploration technology from the University of Chinese Academy of Sciences, Beijing, China, in 2012 and 2015, respectively.

In 2015, he joined the GNSS Remote Sensing Group, National Space Science Center, Chinese Academy of Sciences, Beijing, China, as an Assistant Researcher, where he has been an Associate Professor since 2019. His current research interests include GNSS reflection remote sensing and application, electromagnetic scattering models for sea and bare soil surfaces and their inversion, electromagnetic wave propagation.

Weihua Bai received the Ph.D. degree in space physics from the University of Chinese Academy of Sciences (UCAS), Beijing, China, in 2008. He is currently a Professor with National Space Science Center, Chinese Academy of Sciences, Beijing, China.

Prof. Bai is the Director or Deputy Director in FY3 series GNOS and GNOS-II missions.

His current research interests include GNSS radio occultation and GNSS-R remote sensing techniques, and their applications.

Cong Yin received the B.S., M.S., and Ph.D. degrees in atmosphere physics from the Nanjing University of Information Science and Technology, Nanjing, China, in 2008, 2011, and 2019, respectively.

She is currently a Postdoctoral Fellow with the National Space Science Center, Chinese Academy of Sciences, Beijing, China. Her research focuses on earth surface remote sensing with GNSS-R techniques.

Yueqiang Sun received the B.S. degree in radio physics from Nanjing University, Nanjing, Jiangsu, China, in 1985 and the Ph.D. degree in space physics from the University of Chinese Academy of Sciences (UCAS), Beijing, China, in 2002. He is currently a Professor with the National Space Science Center, Chinese Academy of Sciences, Beijing, China. He devotes to develop GNSS remote sensing and spaceborne spatial environment exploration technologies. She has been the Principal Investigator or Vice Principal Investigator of more than 20 missions/projects in manned space flight, FengYun, and National Natural Science Foundation (863) areas. Her research interests include GNSS radio occultation, GNSS-R remote sensing techniques, atmospheric physics, ionospheric physics, magnetic physics, and space physics.

Xiaochun Zhai was born in Shandong, China, in 1991. She received the B.S. degree in marine technology and the Ph.D. degree in ocean detection technology from the Ocean University of China, Qingdao, China, in 2014 and 2020, respectively.

From 2018 to 2019, she was a joint Ph.D. Student with the Institute of Atmospheric Physics, Germany Aerospace Center (IPA-DLR), with funding from the China Scholarship council. Since July 2020, she has been an Engineer with Satellite Meteorological Institute, National Satellite Meteorological Center, China Meteorological Administration. Her research focuses on the monitoring of sea surface wind and sea ice using microwave remote sensing.

Qifei Du received the Ph.D. degree in space physics from the University of Chinese Academy of Sciences (UCAS), Beijing, China, in 2012. He is currently a Professor with National Space Science Center, Chinese Academy of Sciences, Beijing, China. He was the Principal Investigator of the occultation payloads for Yinghuo satellite and Fengyun-3 satellites. His research interests include spaceborne applications of GNSS signal, including GNSS occultation and GNSS-R remote sensing, GNSS receiver, antenna, and microwave circuits development.

Mi Liao received the bachelor's degree in atmospheric science from the Ocean University of China, Qingdao, China, in 2008, the M.S. degree in atmospheric physics from the Chinese Academy of Meteorological Sciences, Beijing, China, in 2011, and the Ph.D. degree in atmospheric remote sensing and sounding with the Nanjing University of Information Science and Technology, Nanjing, China, in 2020.

She is currently a Senior Engineer with National Satellite Meteorological Center, Beijing, China. Her research interests include radio occultation, ocean monitoring, and products validation.

Lichang Duan received the bachelor's degree in surveying and mapping engineering from the School of Geodesy and Geomatics, Wuhan University, Wuhan, China, in 2020. He is currently working toward the Ph.D. degree in electronic information with the National Space Science Center, University of Chinese Academy of Sciences, Beijing, China.

His research focuses on GNSS-R altimetry inversion.

Xiuqing (Scott) Hu received the B.S. degree in atmospheric science from Nanjing University, Nanjing, China, in 1996, the M.S. degree in cartography and geographical information system from Beijing Normal University, Beijing, China, in 2004, and the Ph.D. degree in quantitative remote sensing science from the Institute of Remote Sensing Application, Chinese Academy of Sciences, Beijing, China, in 2012.

He is currently the Chief Engineering of ground segment system for Fengyun-3 polar-orbiting satellites and the Team Leader of satellites calibration/calibration of National Satellite Meteorological Center, China Meteorological Administration (NSMC/CMA). Since 2010, he has been a Professor of engineering. Since 2015, he has been selected the Technological Leading Talent of CMA.

Dr. Hu was the Chair of GSICS Research Working Group.

Yan Liu received the B.S. degree in atmospheric science and the M.S. degree in meteorology from the Nanjing Institute of Meteorology, Nanjing, China, in 1995 and 2000, respectively, and the Ph.D. degree in meteorology from the Chinese Academy of Meteorological Sciences, Beijing, China, in 2003.

She is currently a Researcher with the Center for Earth System Modeling and Prediction of China Meteorological Administration, Beijing, China. Her research interests include assimilation of GNSS remote sensing data and development of data assimilation system.

Peng Zhang received the master's degree in atmospheric optics from the Anhui Institute of Optics and Fine Mechanics, Chinese Academy of Sciences, Beijing, China, in 1995, and the Ph.D degree in atmospheric physics from the Institute of Atmospheric Physics, Chinese Academy of Sciences, in 1998.

Since 2013, he has been the Deputy Director General of National Satellite Meteorological Centerand Chief Director of FY-3 ground segment. From 2014 to 2017, he was the Chair of Global Space Inter-Calibration System Executive Panel. Since 2015, he has been the Chief Director of Chinese TanSat satellite ground segment. He has the intensive experience in conceiving, developing, and operating FY-3 satellite ground segment. His research interests include the atmospheric remote sensing, satellite data assimilation, and satellite calibration and validation.